Article

CHGNet as a pretrained universal neural network potential for charge-informed atomistic modelling

Bowen Deng[1,2], Peichen Zhong [1,2] ✉, KyuJung Jun [1,2], Janosh Riebesell[2,3], Kevin Han[2], Christopher J. Bartel [1,4] & Gerbrand Ceder [1,2] ✉

Large-scale simulations with complex electron interactions remain one of the greatest challenges for atomistic modelling. Although classical force fields often fail to describe the coupling between electronic states and ionic rearrangements, the more accurate ab initio molecular dynamics suffers from computational complexity that prevents long-time and large-scale simulations, which are essential to study technologically relevant phenomena. Here we present the Crystal Hamiltonian Graph Neural Network (CHGNet), a graph neural network-based machine-learning interatomic potential (MLIP) that models the universal potential energy surface. CHGNet is pretrained on the energies, forces, stresses and magnetic moments from the Materials Project Trajectory Dataset, which consists of over 10 years of density functional theory calculations of more than 1.5 million inorganic structures. The explicit inclusion of magnetic moments enables CHGNet to learn and accurately represent the orbital occupancy of electrons, enhancing its capability to describe both atomic and electronic degrees of freedom. We demonstrate several applications of CHGNet in solid-state materials, including charge-informed molecular dynamics in Li_xMnO_2, the finite temperature phase diagram for Li_xFePO_4 and Li diffusion in garnet conductors. We highlight the significance of charge information for capturing appropriate chemistry and provide insights into ionic systems with additional electronic degrees of freedom that cannot be observed by previous MLIPs.

Large-scale simulations, such as molecular dynamics (MD), are essential tools in the computational exploration of solid-state materials[1]. They enable the study of reactivity, degradation, interfacial reactions, transport in partially disordered structures and other heterogeneous phenomena relevant for the application of complex materials in technology. Technological relevance of such simulations requires rigorous chemical specificity, which originates from the orbital occupancy of atoms. Despite their importance, accurate modelling of electron interactions or their subtle effects in MD simulations remains a major challenge. Classical force fields treat the charge as an atomic property that is assigned to every atom a priori[2,3]. Methodology developments in the field of polarizable force fields such as the electronegativity equalization method[4], chemical potential equalization[5] and charge equilibration[6] realize charge evolution via the redistribution of

[1]Department of Materials Science and Engineering, University of California Berkeley, Berkeley, CA, USA. [2]Materials Sciences Division, Lawrence Berkeley National Laboratory, Berkeley, CA, USA. [3]Cavendish Laboratory, University of Cambridge, Cambridge, UK. [4]Department of Chemical Engineering and Materials Science, University of Minnesota, Minneapolis, MN, USA. ✉e-mail: zhongpc@berkeley.edu; gceder@berkeley.edu

atomic partial charge. However, these empirical methods are often not accurate enough to capture complex electron interactions.

Ab initio molecular dynamics (AIMD) with density functional theory (DFT) can produce high-fidelity results with quantum-mechanical accuracy by explicitly computing the electronic structure within the density functional approximation. The charge-density distribution and corresponding energy can be obtained by solving the Kohn–Sham equation[7]. Long-time and large-scale spin-polarized AIMD simulations critical for studying ion migrations, phase transformations and chemical reactions are challenging and extremely computing intensive[8,9]. These difficulties underscore the need for more efficient computational methods in the field that can account for charged ions and their orbital occupancy at sufficient time and length scales needed to model important phenomena.

Machine-learning interatomic potentials (MLIPs) such as ænet[10,11] and DeepMD[12] have provided promising solutions to bridge the gap between expensive electronic structure methods and efficient classical interatomic potentials. Specifically, graph neural network (GNN)-based MLIPs such as DimeNet[13], NequIP[14], TeaNet[15] and MACE[16] have been shown to achieve state-of-the-art performance by incorporating invariant/equivariant symmetry constraints and long-range interaction through graph convolution[17]. Most recently, GNN-based MLIPs trained on the periodic table (for example, M3GNet) have demonstrated the possibility of universal interatomic potentials that may not require chemistry-specific training for each new application[18–20]. However, the inclusion of the important effects that valences have on chemical bonding remains a challenge for MLIPs, and the early success derived mostly from the inclusion of electrostatics for long-range interactions[21–23].

The importance of an ion's valence derives from the fact that it can engage in very different bonding with its environment depending on its electron count. While traditional MLIPs treat the elemental label as the basic chemical identity, different valence states of transition-metal ions behave as different from each other as different elements. For example, high-spin Mn^{4+} is a non-bonding spherical ion that almost always resides in octahedral coordination by oxygen atoms, whereas Mn^{3+} is a Jahn–Teller active ion that radically distorts its environment, and Mn^{2+} is an ion that strongly prefers tetrahedral coordination[8]. Such strong chemical interaction variability across different valence states exists for almost all transition-metal ions and requires specification of an ion beyond its chemical identity. In addition, the charge state is a degree of freedom that can create configurational entropy and whose dynamic optimization can lead to strongly coupled charge and ion motion, which is impossible to capture with an MLIP that carries only elemental labels. The relevance of explicit electron physics motivates the development of a robust MLIP model with charge information built in.

Charge has been represented in a variety of ways, from a simple oxidation state label to continuous-wave functions derived from quantum mechanics[24]. Challenges in incorporating charge information into MLIPs arise from many factors, such as the ambiguity of representations[25], complexity of interpretation[26], scarcity of labels[22] and impracticality of taking charge as an input for energy calculation ($E(\{\mathbf{r}_i\}, \{q_i\})$), as the charge labels $\{q_i\}$ are generally not a priori available as position labels $\{\mathbf{r}_i\}$)[21]. In this work, we define charge as an atomic property (atomic charge) that can be inferred from the inclusion of magnetic moments (magmoms). We show that by explicitly incorporating the site-specific magmoms as the charge-state constraints into the Crystal Hamiltonian Graph Neural Network (CHGNet), one can both enhance the latent-space regularization and accurately capture electron interactions.

We demonstrate the charge constraints and latent-space regularization of atomic charge in $Na_2V_2(PO_4)_3$ and show the applications of CHGNet in the study of charge transfer and phase transformation in Li_xMnO_2, electronic entropy in the Li_xFePO_4 phase diagram, and lithium (Li) diffusivity in garnet-type Li superionic conductors $Li_{3+x}La_3Te_2O_{12}$. By critically comparing and evaluating the importance of incorporating

charge information in the construction of CHGNet, we offer insights into the materials modelling of ionic systems with additional electronic degrees of freedom. Our analysis highlights the essential role that charge information has in atomistic simulations for solid-state materials.

Results

CHGNet architecture
The foundation of CHGNet is a GNN, as shown in Fig. 1, where the graph convolution layer is used to propagate atomic information via a set of nodes $\{v_i\}$ connected by edges $\{e_{ij}\}$. The translation, rotation and permutation invariance are preserved in GNNs[27–29]. Figure 1a shows the workflow of CHGNet, which takes a crystal structure with unknown atomic charges as input and outputs the corresponding energy, forces, stress and magmoms. The charge-decorated structure can be inferred from the on-site magmoms and atomic orbital theory. The details are described in the following section.

In CHGNet, a periodic crystal structure is converted into an atom graph G^a by searching for neighbouring atoms v_j within r_{cut} of each atom v_i in the primitive cell. The edges e_{ij} are drawn with information from the pairwise distance between v_i and v_j, as shown in Fig. 1b. Three-body interaction can be computed by using an auxiliary bond graph G^b, which can be similarly constructed by taking the angle a_{ijk} as the pairwise information between bonds e_{ij} and e_{jk} (Methods). We adopt similar approaches to include the angular/three-body information as other recent GNN MLIPs[13,18,30]. Figure 1c shows the architecture of CHGNet, which consists of a sequence of basis expansions, embeddings, interaction blocks and output layers (see Methods for details). Figure 1d illustrates the components within an interaction block, where the atomic interaction is simulated with the update of atom, bond and angle features via the convolution layers. Figure 1e presents the convolution layer in the atom graph. Weighted message passing is used to propagate information between atoms, where the message weight $\mathbf{e}_{ij}^a$ from node j to node i decays to zero at the graph cut-off radius to ensure smoothness of the potential energy surface[13].

Unlike other GNNs, where the updated atom features $\{\mathbf{v}_i^t\}$ after t convolution layers are directly used to predict energies, CHGNet regularizes the node-wise features $\{\mathbf{v}_i^{t-1}\}$ at the $t-1$ convolution layer to contain the information about magmoms. The regularized features $\{\mathbf{v}_i^{t-1}\}$ carry rich information about both local ionic environments and charge distribution. Therefore, the atom features $\{\mathbf{v}_i^t\}$ used to predict energy, force and stress are charge constrained by their charge-state information. As a result, CHGNet can provide charge-state information using only the nuclear positions and atomic identities as input, allowing the study of charge distribution in atomistic modelling.

Materials Project Trajectory Dataset
The Materials Project Database contains a vast collection of DFT calculations on ~146,000 inorganic materials composed of 89 elements[31]. To accurately sample the universal potential energy surface, we extracted ~1.37 million structure relaxation and static calculations tasks from the Materials Project Database, using either the generalized gradient approximation (GGA) or GGA + U exchange correlation (Methods). This effort resulted in a comprehensive Materials Project Trajectory (MPtrj) Dataset with 1,580,395 atom configurations, 1,580,395 energies, 7,944,833 magmoms, 49,295,660 forces and 14,223,555 stresses. To ensure the consistency of energies within the MPtrj Dataset, we applied the GGA/GGA + U mixing compatibility correction, as described in ref. 32.

The distribution of elements in the MPtrj Dataset is illustrated in Fig. 2. The lower-left triangle (warm colour) in an element's box indicates the frequency of occurrence of that element in the dataset, and the upper-right triangle (cold colour) represents the number of instances where magnetic information is available for the element. With over 100,000 occurrences for 60 different elements and more than 10,000 instances with magnetic information for 76 different
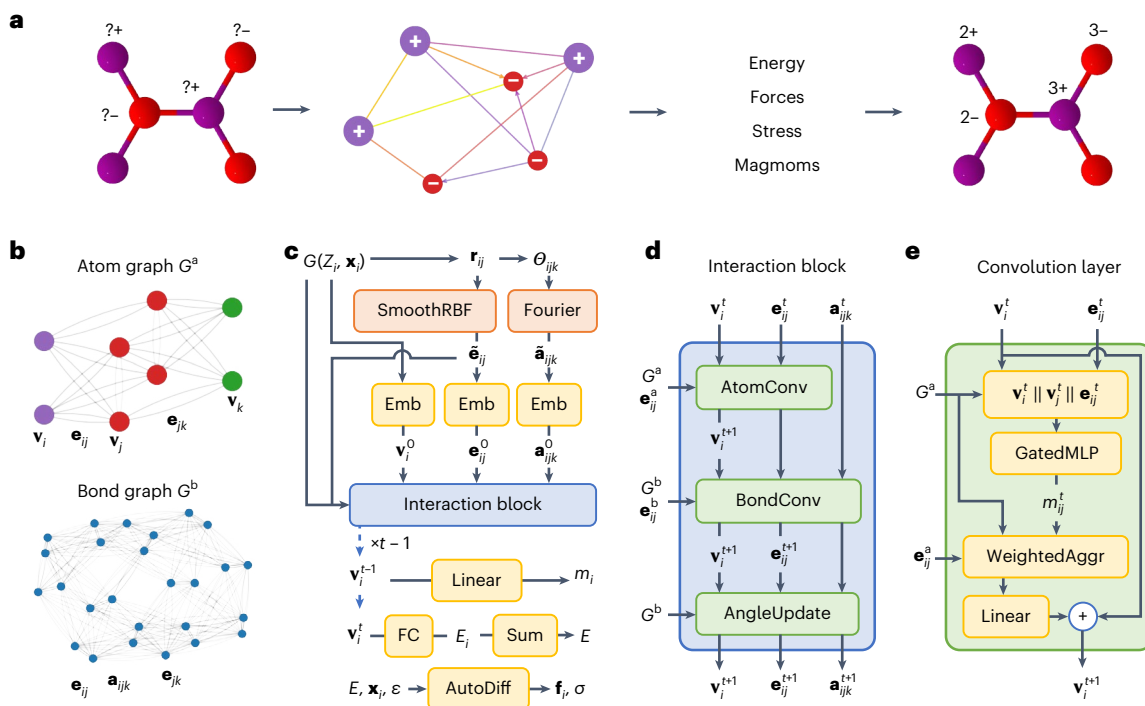
Fig. 1 | CHGNet model architecture. a, CHGNet workflow: a crystal structure with unknown atomic charge is used as input to predict the energy, force, stress and magmoms, resulting in a charge-decorated structure. **b**, Atom graph: the pairwise bond information is drawn between atoms. Bond graph: the pairwise angle information is drawn between bonds. **c**, Graphs run through basis expansions and embedding layers to create atom, bond and angle features.

The features are updated through several interaction blocks, and the properties are predicted at output layers, where FC denotes a nonlinear fully connected layer. **d**, Interaction block in which the atom, bond and angle share and update information. **e**, Atom convolution layer where neighbouring atom and bond information is calculated through weighted message passing and aggregates to the atoms.
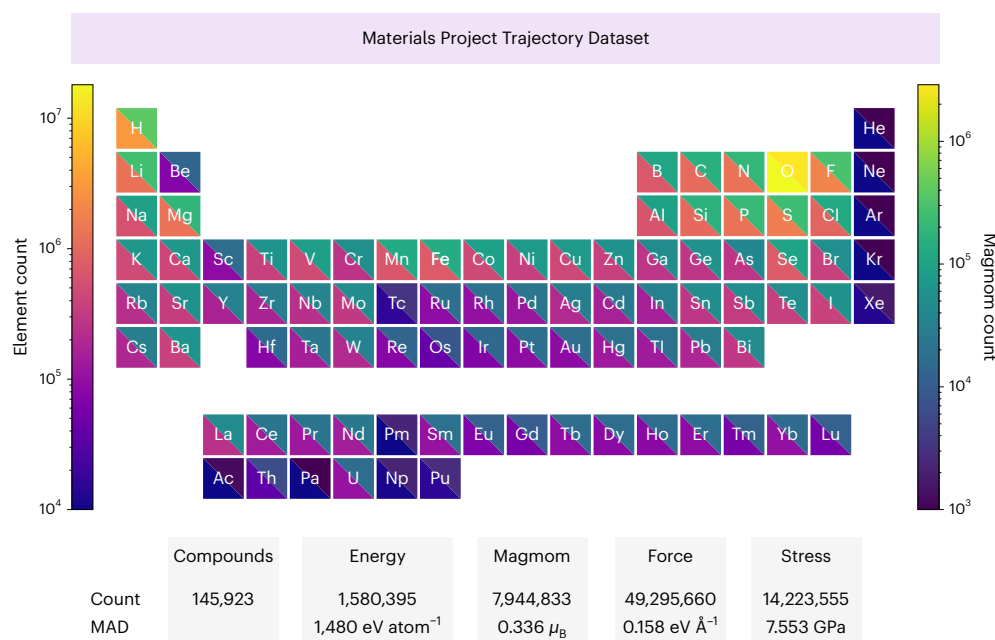
Fig. 2 | Element distribution of the MPtrj Dataset. The colour on the lower-left triangle indicates the total number of atoms/ions of an element. The colour on the upper right indicates the number of times the atoms/ions are incorporated with magmom labels in the MPtrj dataset. On the lower part of the plot is the count and mean absolute deviation (MAD) of energy, magmoms, force and stress.

elements, the MPtrj Dataset provides comprehensive coverage of all chemistries, excluding only the noble gases and actinoids. The lower boxes in Fig. 2 present the counts and mean absolute deviations of energy, force, stress and magmoms in the MPtrj Dataset.

Performance evaluation

CHGNet with 400,438 trainable parameters was trained on the MPtrj Dataset with an 8:1:1 training, validation and test set ratio, partitioned by materials (Methods). Without training on magmom, we achieved

33 meV per atom, 79 meV Å⁻¹ and 0.351 GPa mean absolute errors for energy, force and stress on the MPtrj test set of 157,955 structures from 14,572 materials. With magmom loss included during training, we achieved an improved mean absolute errors of 30 meV per atom, 77 meV Å⁻¹, 0.348 GPa and 0.032 μ_B (Bohr magneton) for energy, force, stress and magmom, correspondingly.

To evaluate the robustness of CHGNet as a universal force field, we submitted CHGNet to Matbench Discovery[33] for out-of-distribution material stability prediction. CHGNet achieves state-of-the-art performance in high-throughput stable inorganic crystal discovery compared with eight other models submitted to this benchmark at the time of writing (Supplementary Fig. 1).

For a benchmark on CHGNet MD simulations, we applied the pretrained CHGNet to MD simulations on Li superionic conductors that were previously reported with AIMD[34]. Supplementary Fig. 2 shows that CHGNet systematically agrees with AIMD results on room temperature conductivities and activation energies across various structures and compositions within the AIMD error bar, and CHGNet successfully distinguishes the faster and slower conductors that were identified with DFT.

Charge constraints and charge inference from magnetic moments

In solid-state materials that contain heterovalent ions, it is crucial to distinguish the atomic charge of the ions, as an element's interaction with its environment can depend strongly on its valence state. It is well known that the valence of heterovalent ions cannot be directly calculated through the DFT charge density because the charge density is almost invariant to the valence state due to the hybridization shift with neighbouring ligand ions[35,36]. Furthermore, the accurate representation and encoding of the full charge density is another demanding task requiring substantial computational resources[26,37]. An established approach is to rely on the magmom for a given atom site as an indicator of its atomic charge, which can be derived from the difference in localized up-spin and down-spin electron densities in spin-polarized DFT calculations[8,38]. Compared with the direct use of charge density, magmoms are found to contain more comprehensive information regarding the electron orbital occupancy and, therefore, the chemical behaviour of ions, as demonstrated in previous studies.

To rationalize our treatment of the atomic charge, we used a NASICON-type Na-ion cathode material $Na_4V_2(PO_4)_3$ as an illustrative example. The phase stability of the (de-)intercalated material $Na_{4-x}V_2(PO_4)_3$ is associated with Na/vacancy ordering and is highly correlated to the charge ordering on the V sites[39]. We generated a supercell structure of $Na_4V_2(PO_4)_3$ with 2,268 atoms and randomly removed half of the Na ions to generate the structure with composition $Na_2V_2(PO_4)_3$, where half of the V ions are oxidized to a V^{4+} state. We used CHGNet to relax the (de-)intercalated structure and analyse its capability to distinguish the valence states of V atoms with the ionic relaxation (Methods).

Figure 3a shows the distribution of predicted magmoms on all V ions in the unrelaxed (blue) and relaxed (orange) structures. Without any prior knowledge about the V-ion charge distribution other than learning from the spatial coordination of the V nuclei, CHGNet successfully differentiates the V ions into two groups of V^{3+} and V^{4+}. Figure 3b shows the two-dimensional principal component analysis (PCA) of all the latent-space feature vectors of V ions for both unrelaxed and relaxed structures after three interaction blocks. The PCA analysis shows two well-separated distributions, indicating the latent-space feature vectors of V ions are strongly correlated to the different valence states of V. Hence, imposing different magmom labels to the latent space (that is, forcing the two orange peaks to converge to the red dashed lines in Fig. 3a) would act as the charge constraints for the model by regularizing the latent-space features.

Because energy, force and stress are calculated from the same feature vectors, the inclusion of magmoms can improve the featurization
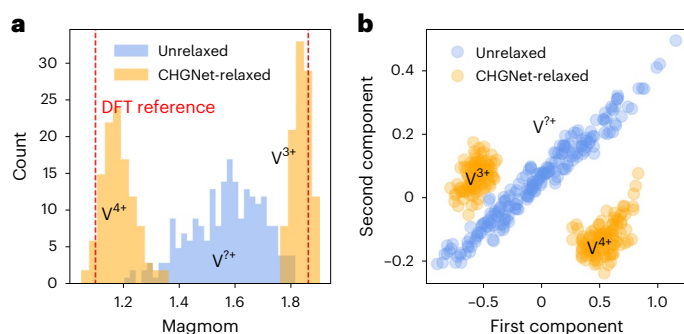
Fig. 3 | Magmom and hidden-space regularization in $Na_2V_2(PO_4)_3$. a, Magmom distribution of the 216 V ions in the unrelaxed structure (blue) and CHGNet-relaxed structure (orange). **b**, A two-dimensional visualization of the PCA on V-ion embedding vectors before the magmom projection layer indicates the latent-space clustering is highly correlated with magmoms and charge information. The PCA reduction is calculated for both unrelaxed and relaxed structures.

of the heterovalent atoms in different local chemical environments (for example, V^{3+} and V^{4+} show very distinct physics and chemistry) and therefore improve the accuracy and expressibility of CHGNet.

Charge disproportionation in Li_xMnO_2 phase transformation

The long-time and large-scale simulation of CHGNet enables studies of ionic rearrangements coupled with charge transfer[40,41], which is crucial for ion mobility and the accurate representation of the interaction between ionic species. As an example, in the $LiMnO_2$ battery cathode material, transition-metal migration has a central role in its phase transformations, which cause irreversible capacity loss[42,43]. The mechanism of Mn migration is strongly coupled with charge transfer, with Mn^{4+} being an immobile ion, and Mn^{3+} and Mn^{2+} generally considered to be more mobile[44–46]. The dynamics of the coupling of the electronic degrees of freedom with those of the ions has been challenging to study but is crucial to understand the phase transformation from orthorhombic $LiMnO_2$ (o-LMO, shown in Fig. 4a) to spinel $LiMnO_2$ (s-LMO), as the timescale and computational cost of such phenomena are far beyond any possible ab initio methods.

In early quasi-static ab initio studies, ref. 40 rationalized the remarkable speed at which the phase transformation proceeds at room temperature using a charge disproportionation mechanism: $2Mn^{3+}_{oct} \rightarrow Mn^{2+}_{tet} + Mn^{4+}_{oct}$, where the subscript indicates location in the tetrahedral (tet) or octahedral (oct) site of a face-centred cubic oxygen packing, as shown in Fig. 4a. The hypothesis based on DFT calculations was that Mn^{2+} had a lower energy barrier for migration between tetrahedral and octahedral sites and preferred to occupy the tetrahedral site. The ability therefore for Mn to dynamically change its valence would explain its remarkable room temperature mobility. However, ref. 44 showed in a later magnetic characterization experiment that the electrochemically transformed spinel $LiMnO_2$ has lower-spin (high-valence) Mn ions on the tetrahedral sites, which suggested the possibility that Mn with higher valence can be stable on tetrahedral sites during the phase transformation.

To demonstrate the ability of CHGNet to fully describe such a process, we used the pretrained CHGNet to run a charge-informed MD simulation at 1,100 K for 1.5 ns (Methods). The MD simulation started from a partially delithiated supercell structure with the o-LMO structure ($Li_{20}Mn_{40}O_{80}$), which is characterized by peaks at 15°, 26° and 40° in the X-ray diffraction (XRD) pattern (the bottom line in Fig. 4b). As the simulation proceeded, a phase transformation from orthorhombic ordering to spinel-like ordering was observed. Figure 4b shows the simulated XRD pattern of MD structures at different time intervals
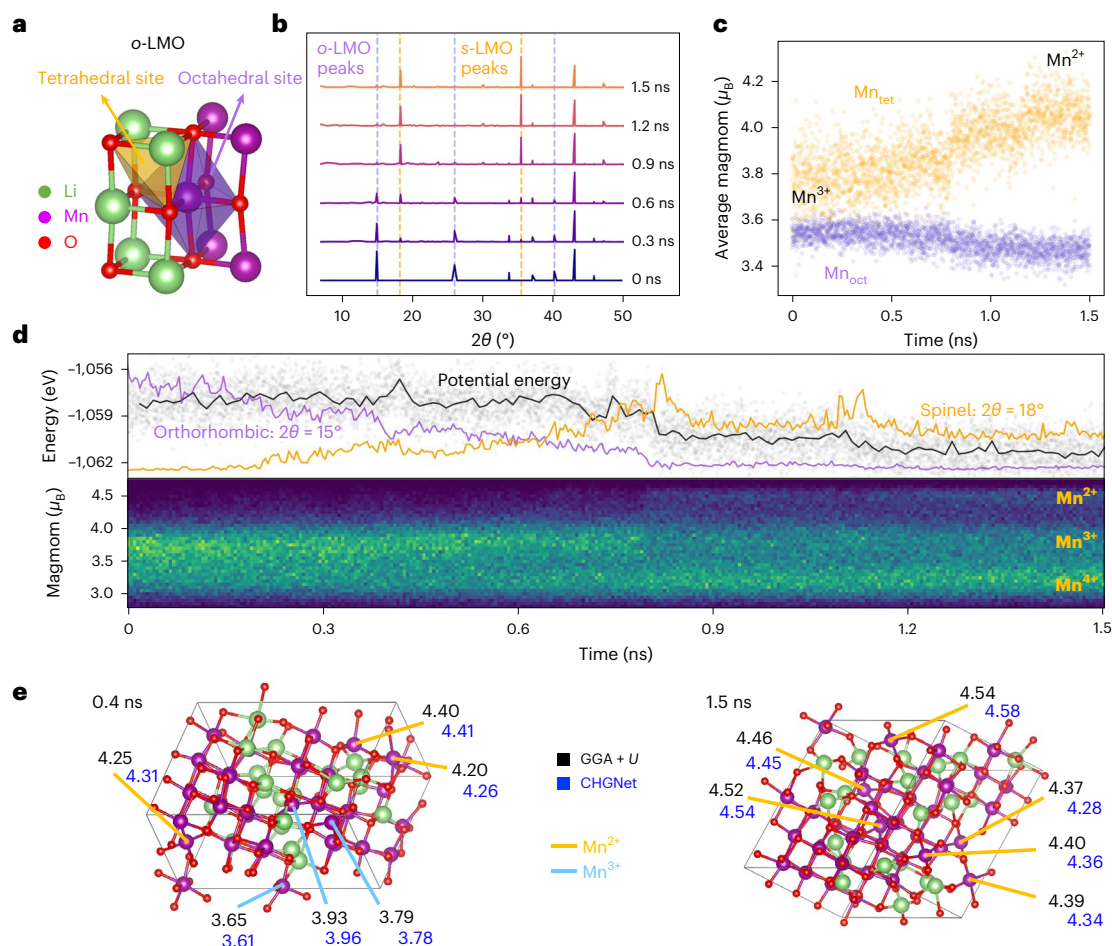
Fig. 4 | Li$_{0.5}$MnO$_2$ phase transformation and charge disproportionation.
a, *o*-LMO unit cell plotted with the tetrahedral site and the octahedral site.
b, Simulated XRD pattern of CHGNet MD structures as the system transforms from the *o*-LMO phase to the *s*-LMO. **c**, Average magmoms of tetrahedral and octahedral Mn ions versus time. **d**, Top: total potential energy and the relative intensity of *o*-LMO and *s*-LMO characteristic peaks versus time. The solid black line is averaged over every 10 ps. Bottom: the histogram of magmoms on all Mn ions versus time. The brighter colour indicates more Mn ions distributed at the magmom. **e**, Predicted magmoms (μ_B) of tetrahedral Mn ions using GGA + *U*-DFT (black) and CHGNet (blue), where the structures are drawn from MD simulation at 0.4 ns (left) and 1.5 ns (right).

from 0 to 1.5 ns, with a clear increase in the characteristic spinel peaks (18°, 35°) and a decrease in the orthorhombic peak. The simulated results agree well with the experimental in situ XRD results[42,44].

Figure 4d shows the CHGNet-predicted energy of the LMO super-cell structure as a function of simulation time, together with the peak strength at $2\theta = 15°$ and 18°. An explicit correlation between the structural transformation and energy landscape is observed. The predicted average potential energy of the spinel phase is approximately 50 meV per oxygen lower than that of the starting *o*-LMO, suggesting that the phase transformation to spinel is indeed thermodynamically favoured.

The advantage of CHGNet is shown in its ability to predict charge-coupled physics, as evidenced by the lower plot in Fig. 4d. A histogram of the magmoms of all the Mn ions in the structure is presented against time. In the early part of the simulation, the magmoms of Mn ions are mostly distributed between $3\,\mu_B$ and $4\,\mu_B$, which correspond to Mn^{4+} and Mn^{3+}. At approximately 0.8 ns, there is a significant increase in the amount of Mn^{2+}, which is accompanied by a decrease in the potential energy and increase in the spinel XRD peaks. Following this major transformation point, the Mn^{3+} ions undergo charge disproportionation, resulting in the coexistence of Mn^{2+}, Mn^{3+} and Mn^{4+} in the transformed spinel-like structure.

One important observation from the long-time charge-informed MD simulation is the correlation between ionic rearrangements and the charge-state evolution. Specifically, we noticed that the timescale of charge disproportionation (approximately nanoseconds for the emergence of Mn^{2+}) is far longer than the timescale of ion hops (approximately picoseconds for the emergence of Mn_{tet}), indicating that the migration of Mn to the tetrahedral coordination is less likely related to the emergence of Mn^{2+}. Instead, our result indicates that the emergence of Mn^{2+}_{tet} is correlated to the formation of the long-range spinel-like ordering. Figure 4c shows the average magmoms of Mn_{tet} and Mn_{oct} as a function of time. The result reveals that Mn^{2+}_{tet} only forms over a long time period, which cannot be observed using any conventional simulation techniques.

To further validate this hypothesis and the accuracy of CHGNet prediction, we used GGA + *U* and r^{2}SCAN-DFT (Supplementary Fig. 3) static calculations to get the magmoms of the structures at 0.4 ns and 1.5 ns, where the GGA + *U* results are shown in Fig. 4e. CHGNet (blue) shows highly accurate agreements with GGA + *U* magmoms (black) and infers the same Mn_{tet} valence states.

Electronic entropy effect in the phase diagram of Li$_x$FePO$_4$
The configurational electronic entropy has a significant effect on the temperature-dependent phase stability of mixed-valence oxides, and its equilibrium modelling, therefore, requires an explicit indication of the atomic charge. However, no current MLIPs can provide such
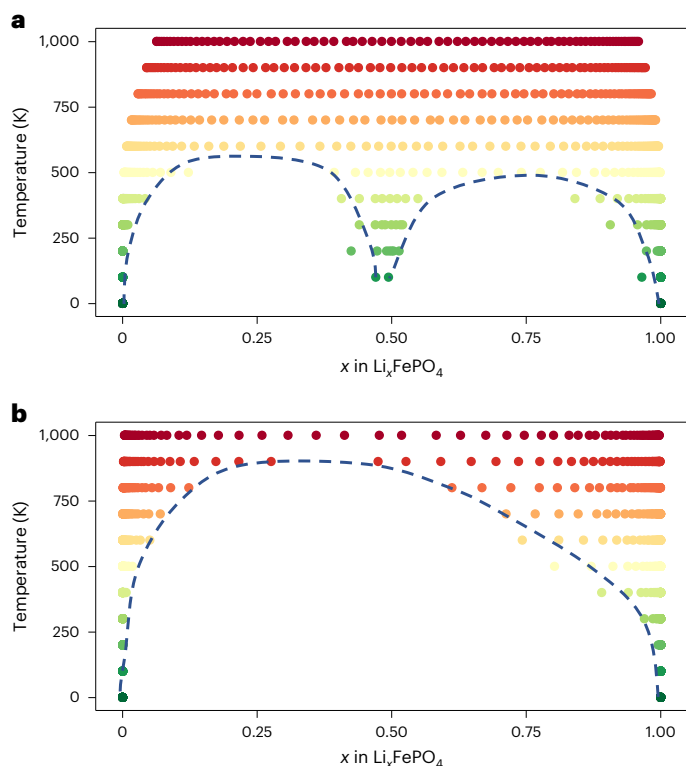
Fig. 5 | Li_xFePO_4 phase diagrams from CHGNet. a,b, The phase diagrams are calculated with **(a)** and without **(b)** electronic entropy on Fe^{2+} and Fe^{3+}. The coloured dots represent the stable phases obtained in semigrand canonical MC. The dashed lines indicate the two-phase equilibria between solid solution phases.

Fig. 6 | Li diffusivity in garnet $Li_3La_3Te_2O_{12}$. The CHGNet simulation accurately reproduces the dramatic increase in Li-ion diffusivity (D) when a small amount of extra Li is stuffed into the garnet structure, qualitatively matching the activated diffusion network theory and agreeing well with the DFT-computed activation energy (E_a). The unstuffed $Li_3La_3Te_2O_{12}$ structure is shown for reference.

information. We demonstrate that using CHGNet, one can infer the atomic charge and include the electronic entropy in the computation of the temperature-dependent phase diagram of Li_xFePO_4.

Previous research has shown that the formation of a solid solution in Li_xFePO_4 is mainly driven by electronic entropy rather than by Li^+/vacancy configurational entropy[47]. We applied CHGNet as an energy calculator to generate two distinct cluster expansions, which is a typical approach to studying configurational entropy[48]. One of these is charge decorated (considering Li^+/vacancy and Fe^{2+}/Fe^{3+}) and another is non-charge decorated (only considering Li^+/vacancy without consideration of the Fe valence). Semigrand canonical Monte Carlo was used to sample these cluster expansions and construct Li_xFePO_4 phase diagrams (Methods). The calculated phase diagram with charge decoration in Fig. 5a features a miscibility gap between $FePO_4$ and $LiFePO_4$, with a eutectoid-like transition to the solid solution phase at intermediate Li concentration, qualitatively matching the experiment result[49,50]. In contrast, the calculated phase diagram without charge decoration in Fig. 5b features only a single miscibility gap without any eutectoid transitions, in disagreement with experiments. This comparison highlights the importance of explicit inclusion of the electronic degrees of freedom, as failure to do so can result in incorrect physics. These experiments show how practitioners may benefit from CHGNet with atomic charge inference for equilibrium modelling of configurationally and electronically disordered systems.

Activated Li diffusion network in $Li_3La_3Te_2O_{12}$
In this section, we showcase the precision of CHGNet for general-purpose MD. Lithium-ion diffusivity in fast Li-ion conductors is known to show a drastic nonlinear response to compositional change. For example, stuffing a small amount of excess Li into stoichiometric compositions can result in orders-of-magnitude improvement of the ionic

conductivity[34]. A previous study[51] reported that the activation energy of Li diffusion in stoichiometric garnet $Li_3La_3Te_2O_{12}$ decreases from more than 1 eV to ~160 meV in a slightly stuffed $Li_{3+\delta}$ garnet ($\delta = 1/48$), owing to the activated Li diffusion network of face-sharing tetrahedral and octahedral sites.

We performed a zero-shot test to assess the ability of CHGNet to capture the effect of such slight compositional change on the diffusivity and its activation energy. Figure 6 shows the Arrhenius plot from CHGNet-based MD simulations and compares it with AIMD results. Our results indicate that not only is the activated diffusion network effect precisely captured but also the activation energies from CHGNet are in excellent agreement with the DFT results[51]. This effort demonstrates the capability of CHGNet to precisely capture the strong interactions between Li ions in activated local environments and the ability to simulate highly nonlinear diffusion behaviour. Moreover, CHGNet can dramatically decrease the error on simulated diffusivity and enable studies in systems with poor diffusivity such as the unstuffed Li_3 garnet by extending to nanosecond-scale simulations[52].

Discussion
Large-scale computational modelling has proven essential in providing atomic-level information in materials science, medical science and molecular biology. Many technologically relevant applications contain heterovalent species, for which a comprehensive understanding of the atomic charge involved in the dynamics of processes is of great interest. The importance of assigning a valence to ions derives from the fundamentally different electronic and bonding behaviour ions can exhibit when their electron count changes. Ab initio calculations based on DFT are useful for these problems, but the $\sim \mathcal{O}(N^3)$ scaling intrinsically prohibits its application to large time and length scales. Recent development of MLIPs provides opportunities to increase computational efficiency while maintaining near DFT accuracy. The present work presents an MLIP that combines the need to include the electronic degrees of freedom with computational efficiency.

In this work, we developed CHGNet and demonstrated the effectiveness of incorporating magmoms as a proxy for inferring the atomic charge in atomistic simulations, which results in the integration of electronic information and the imposition of additional charge constraints as a regularization of the MLIP. We highlight the capability of CHGNet in

distinguishing Fe^{2+}/Fe^{3+} in the study of Li_xFePO_4, which is essential for the inclusion of electronic entropy and finite temperature phase stability. In the study of $LiMnO_2$, we demonstrate CHGNet's ability to gain insights into the relation between charge disproportionation and phase transformation in a heterovalent transition-metal oxide system from long-time charge-informed MD. CHGNet builds on recent advances in graph-based MLIPs[13,18], but is pretrained with electronic degrees of freedom built in, which provides an ideal solution for high-throughput screening and atomistic modelling of a variety of technologically relevant oxides, including high-entropy materials[53,54]. As CHGNet is already generalized to broad chemistry during pretraining, it can also serve as a data-efficient and highly robust model for high-precision simulations when augmented with fine-tuning to specific chemistries (Supplementary Section IV.).

Despite these advances, further improvements can be achieved through several efforts. First, the use of magmoms for valence states inference does not strictly ensure global charge neutrality. The formal valence assignment depends on how the atomic charges are partitioned[24]. Second, although magmoms are good heuristics for the atomic charge from spin-polarized calculations in ionic systems, it is recognized that the atomic charge inference for non-magnetic ions may be ambiguous and thus requires extra domain knowledge. As a result, for ions with no magmom, the atom-centred magmoms cannot accurately reflect their atomic charges and CHGNet will infer charge from the environment similar to how other MLIP's function. It may also be possible to enhance the model further by incorporating other approaches to charge representation, such as an electron localization function[55], electric polarization[56] and atomic orbital-based partitioning (for example, Wannier functions[57]). These approaches could be used for atom feature engineering in latent space.

In conclusion, CHGNet enables charge-informed atomistic simulations amenable to the study of heterovalent systems using large-scale computational simulations, expanding opportunities to study charge-transfer-coupled phenomena in computational chemistry, physics, biology and materials science.

Methods

Data parsing

The MPtrj Dataset was parsed from the September 2022 Materials Project Database version. We collected all the GGA and GGA + U task trajectories under each material-id and followed the criteria below:

(1) We removed deprecated tasks and only kept tasks with the same calculation settings as the primary task, from which the material could be searched on the Materials Project website.
To verify whether the calculation settings were equal, we confirmed the following: (1) the +U setting must be the same as the primary task and (2) the energy of the final frame cannot differ by more than 20 meV per atom from the primary task.
(2) Structures without energy and forces or electronic step convergence were removed.
(3) Structures with energy higher than 1 eV per atom or lower than 10 meV per atom relative to the relaxed structure from Materials Project's ThermoDoc were filtered out to eliminate large energy differences caused by variations in Vienna Ab initio Simulation Package settings and so on.
(4) Duplicate structures were removed to maintain a healthy data distribution. This removal was achieved using a pymatgen StructureMatcher and an energy matcher to tell the difference between structures. The screening criteria of the structure and energy matchers became more stringent as more structures under the same mp-id were added to the MPtrj Dataset.

Training, validation and test sets of the MPtrj dataset were randomly selected based on the 145,923 compounds (based on the mp-id). As a result, different DFT tasks and their trajectory frames can only be included in the same set conditioned on the compound.

Model design

In constructing the crystal graph, the default r_{cut} is set to 5 Å, which has been shown adequate enough for capturing long-range interactions[18]. The bond graph is constructed with a cut-off of 3 Å for computational efficiency. The bond distances r_{ij} are expanded to $\tilde{\mathbf{e}}_{ij}^a$ and $\tilde{\mathbf{e}}_{ij}^b$ for the atom graph and the bond graph, respectively, by a trainable smooth radial Bessel function (SmoothRBF), as proposed in ref. 13. The SmoothRBF constraints the radial Bessel function and its derivative to approach zero at the graph cut-off radius, thus guaranteeing a smooth potential energy surface. The angles θ_{ijk} are expanded by Fourier basis functions to create $\tilde{\mathbf{a}}_{ijk}$ with trainable frequency. The atomic numbers $\mathbf{Z}_{ii}$, $\tilde{\mathbf{e}}_{ij}^a$ and $\tilde{\mathbf{a}}_{ijk}$ are then embedded into node $\mathbf{v}_i^0$, edge $\mathbf{e}_{ij}^0$ and angle features $\mathbf{a}_{ijk}^0$ (all have 64 feature dimensions by default):

$$\mathbf{v}_i^0 = \mathbf{Z}_i\mathbf{W}_v + \mathbf{b}_v, \ \mathbf{e}_{ij}^0 = \tilde{\mathbf{e}}_{ij}^a\mathbf{W}_e, \ \mathbf{a}_{ijk}^0 = \tilde{\mathbf{a}}_{ijk}\mathbf{W}_a$$

$$\mathbf{e}_{ij}^a = \tilde{\mathbf{e}}_{ij}^a\mathbf{W}_{ag}, \ \mathbf{e}_{ij}^b = \tilde{\mathbf{e}}_{ij}^b\mathbf{W}_{bg}$$

$$\tilde{e}_{ij,n}^a = \sqrt{\frac{2}{5}}\frac{\sin\left(\frac{n\pi r_{ij}}{5}\right)}{r_{ij}} \odot u^a(r_{ij})$$

$$\tilde{a}_{ijk,\ell} = \begin{cases} \frac{1}{\sqrt{2\pi}} & \text{if } \ell = 0 \\ \frac{1}{\sqrt{\pi}}\cos[\ell\theta_{ijk}] & \text{if } \ell = [1,N] \\ \frac{1}{\sqrt{\pi}}\sin[(\ell-N)\theta_{ijk}] & \text{if } \ell = [N+1,2N] \end{cases}$$

(1)

where $\{\mathbf{W}, \mathbf{b}\}$ are the trainable weights and bias. The angle is computed using $\theta_{ijk} = \arccos\frac{\mathbf{e}_{ij}\cdot\mathbf{e}_{jk}}{|\mathbf{e}_{ij}||\mathbf{e}_{jk}|}$. The $u^a(r_{ij})$ is a polynomial envelope function to enforce the value, the first and second derivatives of $\tilde{\mathbf{e}}_{ij}^a$ to decay smoothly towards 0 at the atom graph cut-off (u^a) and bond graph cut-off (u^b)[13]. The $\mathbf{e}_{ij}^a$ and $\mathbf{e}_{ij}^b$ vectors are created to ensure a continuous message passing in graph convolutions. The n and ℓ are the expansion orders, and we set the maximum orders for both n and ℓ to be $2N + 1 = 9$. The superscript 0 denotes the index of the interaction block. The $\odot$ represents the element-wise multiplication. The edge vectors $\mathbf{e}_{ij}^t$ are bidirectional, which is essential for $\mathbf{e}_{ij}^t$ and $\mathbf{e}_{ji}^t$ to be represented as a single node in the bond graph[30].

Different from previous GNN models such as M3GNet[18], where three-body spherical harmonics features are used to update bond features, we explicitly encode and update atoms, bonds and angles embeddings through the interaction blocks that operate upon the pairwise connections pre-defined in atom graph and bond graph. For the atom graph convolution, a weighted message passing layer is applied to the concatenated feature vectors $(\mathbf{v}_i^t||\mathbf{v}_j^t||\mathbf{e}_{ij}^t)$ from two atoms and one bond. For the bond graph convolution, the weighted message passing layer is applied to the concatenated feature vectors $(\mathbf{e}_{ij}^t||\mathbf{e}_{jk}^t||\mathbf{a}_{ijk}^t||\mathbf{v}_j^{t+1})$ from two bidirected bonds, the angle between them and the atom where the angle is located. For the angle update function, we used the same construction for the bond graph message vector but without the weighted aggregation step. The mathematical form of the atom, bond and angle updates are formulated below:

$$\mathbf{v}_i^{t+1} = \mathbf{v}_i^t + L_v^t\left[\sum_j \mathbf{e}_{ij}^a \odot \phi_v^t\left(\mathbf{v}_i^t||\mathbf{v}_j^t||\mathbf{e}_{ij}^t\right)\right],$$

$$\mathbf{e}_{jk}^{t+1} = \mathbf{e}_{jk}^t + L_e^t\left[\sum_i \mathbf{e}_{ij}^b \odot \mathbf{e}_{jk}^b \odot \phi_e^t\left(\mathbf{e}_{ij}^t||\mathbf{e}_{jk}^t||\mathbf{a}_{ijk}^t||\mathbf{v}_j^{t+1}\right)\right],$$

$$\mathbf{a}_{ijk,f}^{t+1} = \mathbf{a}_{ijk}^t + \phi_a^t\left(\mathbf{e}_{ij}^{t+1}||\mathbf{e}_{jk}^{t+1}||\mathbf{a}_{ijk}^t||\mathbf{v}_j^{t+1}\right).$$

(2)

The L is a linear layer and ϕ is the gated multilayer perceptron (gatedMLP)[29]:

$$L(\mathbf{x}) = \mathbf{x}\mathbf{W} + \mathbf{b},$$

$$\phi(\mathbf{x}) = (\sigma \circ L_{gate}(\mathbf{x})) \odot (g \circ L_{core}(\mathbf{x})),$$

(3)

where σ and g are the Sigmoid and SiLU activation functions, respectively. The magmoms are predicted by a linear projection of the atom features $\mathbf{v}_i^3$ after three interaction blocks by

$$m_i = L_m(\mathbf{v}_i^3). \qquad (4)$$

After this layer of charge constraints, the final interaction block with only the atom graph convolution updates the atom features. The total energy is then calculated by the sum of the nonlinear projections of final atom features $\{\mathbf{v}_i^4\}$. The forces $\{\mathbf{f}_i\}$ and stress (σ) are calculated via auto-differentiation of the energy with respect to the atomic Cartesian coordinates $\{\mathbf{x}_i\}$ and lattice strain tensor (ε):

$$E_{\text{tot}} = \sum_i L_3 \circ g \circ L_2 \circ g \circ L_1(\mathbf{v}_i^4),$$
$$\mathbf{f}_i = -\frac{\partial E_{\text{tot}}}{\partial \mathbf{x}_i}, \qquad (5)$$
$$\sigma = \frac{1}{V}\frac{\partial E_{\text{tot}}}{\partial \varepsilon}.$$

Overall, with four atom convolution layers, the pretrained CHGNet can capture long-range interaction up to 20 Å with a small computation cost.

Model training

The model is trained to minimize the summation of Huber loss (with $\delta = 0.1$) of energy, force, stress and magmoms:

$$\mathcal{L}(x, \hat{x}) = \begin{cases} 0.5 \cdot (x - \hat{x})^2 & \text{if } |x - \hat{x}| < \delta \\ \delta \cdot (|x - \hat{x}| - 0.5\delta) & \text{otherwise} \end{cases}. \qquad (6)$$

The loss function is a weighted sum of the contributions from energy, forces, stress and magmoms:

$$\mathcal{L} = \mathcal{L}(E, \hat{E}) + w_f\mathcal{L}(\mathbf{f}, \hat{\mathbf{f}}) + w_\sigma\mathcal{L}(\sigma, \hat{\sigma}) + w_m\mathcal{L}(m, \hat{m}), \qquad (7)$$

where the weights for the forces, stress and magmoms are set to $w_f = 1$, $w_\sigma = 0.1$ and $w_m = 0.1$, respectively. The DFT energies are normalized with elemental reference energies before fitting to CHGNet to decrease variances[18]. The absolute values of DFT magmoms are used for training. The batch size is set to 40 and the Adam optimizer is used with 10^{-3} as the initial learning rate. The CosineAnnealingLR scheduler is used to adjust the learning rate 10 times per epoch, and the final learning rate decays to 10^{-5} after 20 epochs.

Software interface

CHGNet was implemented using pytorch 1.12.0[58], with crystal structure processing from pymatgen[59]. MD and structure relaxation were simulated using the interface to Atomic Simulation Environment[60]. The cluster expansions were performed using the smol package[61].

Structure relaxation and molecular dynamics

All the structure relaxations were optimized by the FIRE optimizer over the potential energy surface provided by CHGNet[62], where the atom positions, cell shape and cell volume were simultaneously optimized to reach converged interatomic forces of 0.1 eV Å^{-1}.

For the MD simulations of the o-LMO to s-LMO phase transformation, the initial structure $Li_{20}Mn_{40}O_{80}$ was generated by randomly removing Li from a $Li_{40}Mn_{40}O_{80}$ supercell of the orthorhombic structure and relaxing with DFT. The MD simulation was run under constant number of particles, volume, and temperature (NVT) ensemble, with a time step of 2 fs at temperature $T = 1,100$ K for 1.5 ns. For the simulated XRD in Fig. 4b, the structures at 0.0, 0.3, 0.6, 0.9, 1.2 and 1.5 ns were coarse-grained to their nearest Wyckoff positions to remove noisy peaks. In Fig. 4c, Mn_{oct} and Mn_{tet} were determined by counting the number of bonding oxygen ions within 2.52 Å. If six bonding oxygen ions

are found, then the Mn ion is categorized into Mn_{oct}; if fewer than six bonding oxygen ions are found, the Mn ion is coarse-grained into Mn_{tet} for representation of lower coordinated environments. In Fig. 4e, Mn^{2+} and Mn^{3+} are classified by CHGNet magmom threshold of 4.2 μ_B (ref. 38).

For the MD simulations of garnet $Li_3La_3Te_2O_{12}$ systems, a time step of 2 fs was used. The NVT ensemble was used as the effect of thermal expansion on activation energy is minimal compared with the scale of the activated Li diffusion network. We ramped up the temperature to the targeted temperature in the NVT ensemble with at least 1 ps. Then, after equilibrating the system for 50 ps, the Li self-diffusion coefficients were obtained by calculating the mean squared displacements of trajectories for at least 2.3 ns. The uncertainty analysis of the diffusion coefficient values was conducted following the empirical error estimation scheme proposed in ref. 63. In $Li_{3+\delta}$, the excess lithium was stuffed to an intermediate octahedral (48g) site to face-share with the fully occupied 24d tetrahedral sites.

Phase diagram calculations

The cluster expansions of Li_xFePO_4 were performed with pair interactions up to 11 Å and triplet interactions up to 7 Å based on the relaxed unit cell of $LiFePO_4$. For better energy accuracy, we first fine-tuned CHGNet with the Materials Project structures in the Li–Fe–P–O chemical space, which decreased the test error from 23 meV per atom to 15 meV per atom (Supplementary Section IV). We applied CHGNet to relax 456 different structures in Li_xFePO_4 ($0 \leq x \leq 1$) and predict the energies and magmoms, where the 456 structures were generated via an automatic workflow including cluster expansion fitting, canonical cluster expansion Monte Carlo for searching the ground state at varied Li^+ composition and CHGNet relaxation. The charge-decorated cluster expansion is defined on coupled sublattices over Li^+/vacancy and Fe^{2+}/Fe^{3+} sites, where Fe^{2+} and Fe^{3+} are treated as different species. In addition, the non-charge-decorated cluster expansion is defined only on Li^+/vacancy sites. In the charge-decorated cluster expansion, Fe^{2+}/Fe^{3+} is classified with magmom in [$3\mu_B$, $4\mu_B$] and [$4\mu_B$, $5\mu_B$], respectively[38].

The semigrand canonical Monte Carlo simulations were implemented using the Metropolis–Hastings algorithm, where 20% of the MC steps were implemented canonically (swapping Li^+/vacancy or Fe^{2+}/Fe^{3+}) and 80% of the MC steps were implemented grand-canonically using the table-exchange method[64,65]. The simulations were implemented on an $8 \times 6 \times 4$ of the unit cell of $LiFePO_4$. In each MC simulation, we scanned the chemical potential in the [−5.6, −4.8] range with a step of 0.01 and sampled the temperatures from 0 to 1,000 K. The boundary for the solid solution stable phases is determined with a difference in the Li concentration <0.05 by $\Delta\mu = 0.01$ eV.

The effects of configurational and electronic entropy can be investigated via $S(\text{Li}, e) = S'(\text{Li}) + S'(e) + I(\text{Li}, e)$ as described in ref. 47. S' represents the conditional entropy $S(X|Y)$ from X (either Li or e) degree of freedom given fixed Y (e or Li), and $I(\text{Li}, e)$ denotes the mutual information of the two degrees of freedom. $S'(e/\text{Li})$ can be acquired from a canonical MC with a frozen configuration of either Li/vacancy or Fe^{2+}/Fe^{3+} ordering. This operation is facilitated by explicitly incorporating the charge decoration degree of freedom with the cluster expansion, a necessity substantiated by the atomic charge inference derived from CHGNet.

DFT calculations

DFT calculations were performed with the Vienna Ab initio Simulation Package using the projector-augmented wave method[66,67], a plane-wave basis set with an energy cut-off of 520 eV, and a reciprocal space discretization of 25 k-points per Å^{-1}. All the calculations were converged to 10^{-6} eV in total energy for electronic loops and 0.02 eV Å^{-1} in interatomic forces for ionic loops. We used the Perdew–Burke–Ernzerhof GGA exchange-correlation functional[68] with rotationally averaged Hubbard U correction (GGA + U) to compensate for the self-interaction error on transition-metal atoms (3.9 eV for Mn)[69].

Data availability

The MPtrj dataset used to train CHGNet is available at https://doi.org/10.6084/m9.figshare.23713842 (ref. 70). Source data are provided with this paper.

Code availability

The source code, pretrained weights and example notebooks of CHGNet are available at https://github.com/CederGroupHub/chgnet and https://doi.org/10.5281/zenodo.8173515 (ref. 71).

References

1. Frenkel, D. & Smit, B. *Understanding Molecular Simulation: from Algorithms to Applications* Vol. 1 (Elsevier, 2001).
2. Lucas, T. R., Bauer, B. A. & Patel, S. Charge equilibration force fields for molecular dynamics simulations of lipids, bilayers, and integral membrane protein systems. *Biochim. Biophys. Acta Biomembr.* **1818**, 318–329 (2012).
3. Drautz, R. Atomic cluster expansion of scalar, vectorial, and tensorial properties including magnetism and charge transfer. *Phys. Rev. B* **102**, 024104 (2020).
4. Mortier, W. J., Ghosh, S. K. & Shankar, S. Electronegativity-equalization method for the calculation of atomic charges in molecules. *J. Am. Chem. Soc.* **108**, 4315–4320 (1986).
5. York, D. M. & Yang, W. A chemical potential equalization method for molecular simulations. *J. Chem. Phys.* **104**, 159–172 (1996).
6. Rappe, A. K. & Goddard, W. A. Charge equilibration for molecular dynamics simulations. *J. Phys. Chem.* **95**, 3358–3363 (1991).
7. Kohn, W. & Sham, L. J. Self-consistent equations including exchange and correlation effects. *Phys. Rev.* **140**, A1133 (1965).
8. Reed, J. & Ceder, G. Role of electronic structure in the susceptibility of metastable transition-metal oxide structures to transformation. *Chem. Rev.* **104**, 4513 (2004).
9. Eum, D. et al. Voltage decay and redox asymmetry mitigation by reversible cation migration in lithium-rich layered oxide electrodes. *Nat. Mater.* **19**, 419 (2020).
10. Artrith, N., Morawietz, T. & Behler, J. High-dimensional neural-network potentials for multicomponent systems: applications to zinc oxide. *Phys. Rev. B* **83**, 153101 (2011).
11. Lopez-Zorrilla, J. et al. ænet-PyTorch: a GPU-supported implementation for machine learning atomic potentials training. *J. Chem. Phys.* **158**, 164105 (2023).
12. Zhang, L., Wang, H., Car, R. & E, W. Phase diagram of a deep potential water model. *Phys. Rev. Lett.* **126**, 236001 (2021).
13. Gasteiger, J., Groß, J. & Günnemann, S. Directional message passing for molecular graphs. In *International Conference on Learning Representations* (ICLR, 2020).
14. Batzner, S. et al. E(3)-equivariant graph neural networks for data-efficient and accurate interatomic potentials. *Nat. Commun.* **13**, 2453 (2022).
15. Takamoto, S., Izumi, S. & Li, J. TeaNet: universal neural network interatomic potential inspired by iterative electronic relaxations. *Comput. Mater. Sci.* **207**, 111280 (2022).
16. Batatia, I., Kovacs, D. P., Simm, G. N. C., Ortner, C. & Csanyi, G. in *Advances in Neural Information Processing Systems* (eds Koyejo, S. et al.) 11423–11436 (Curran Associates, 2022).
17. Fu, X. et al. Forces are not enough: benchmark and critical evaluation for machine learning force fields with molecular simulations. *Trans. Mach. Learn. Res.* (2023).
18. Chen, C. & Ong, S. P. A universal graph deep learning interatomic potential for the periodic table. *Nat. Comput. Sci.* **2**, 718–728 (2022).
19. Choudhary, K. et al. Unified graph neural network force-field for the periodic table: solid state applications. *Digit. Discov* **2**, 346–355 (2023).
20. Takamoto, S. et al. Towards universal neural network potential for material discovery applicable to arbitrary combination of 45 elements. *Nat. Commun.* **13**, 2991 (2022).
21. Unke, O. T. et al. SpookyNet: learning force fields with electronic degrees of freedom and nonlocal effects. *Nat. Commun.* **12**, 7273 (2021).
22. Ko, T. W., Finkler, J. A., Goedecker, S. & Behler, J. A fourth-generation high-dimensional neural network potential with accurate electrostatics including non-local charge transfer. *Nat. Commun.* **12**, 398 (2021).
23. Zubatyuk, R., Smith, J. S., Nebgen, B. T., Tretiak, S. & Isayev, O. Teaching a neural network to attach and detach electrons from molecules. *Nat. Commun.* **12**, 4870 (2021).
24. Walsh, A., Sokol, A. A., Buckeridge, J., Scanlon, D. O. & Catlow, C. R. A. Oxidation states and ionicity. *Nat. Mater.* **17**, 958 (2018).
25. Xie, X., Persson, K. A. & Small, D. W. Incorporating electronic information into machine learning potential energy surfaces via approaching the ground-state electronic energy as a function of atom-based electronic populations. *J. Chem. Theor. Comput.* **16**, 4256–4270 (2020).
26. Gong, S. et al. Predicting charge density distribution of materials using a local-environment-based graph convolutional network. *Phys. Rev. B* **100**, 184103 (2019).
27. Bruna, J., Zaremba, W., Szlam, A. & LeCun, Y. Spectral networks and locally connected networks on graphs. In *2nd International Conference on Learning Representations* (ICLR, 2014).
28. Geiger, M. & Smidt, T. e3nn: Euclidean neural networks. Preprint at https://arxiv.org/abs/2207.09453 (2022).
29. Xie, T. & Grossman, J. C. Crystal graph convolutional neural networks for an accurate and interpretable prediction of material properties. *Phys. Rev. Lett.* **120**, 145301 (2018).
30. Choudhary, K. & DeCost, B. Atomistic line graph neural network for improved materials property predictions. *npj Comput. Mater.* **7**, 185 (2021).
31. Jain, A. et al. The Materials Project: a materials genome approach to accelerating materials innovation. *APL Mater.* **1**, 011002 (2013).
32. Wang, A. et al. A framework for quantifying uncertainty in DFT energy corrections. *Sci. Rep.* **11**, 15496 (2021).
33. Riebesell, J., Goodall, R. E. A., Jain, A., Benner, P., Persson, K. A. & Lee, A. A. Matbench Discovery—an evaluation framework for machine learning crystal stability prediction. Preprint at https://arxiv.org/abs/2308.14920 (2023).
34. Jun, K. et al. Lithium superionic conductors with corner-sharing frameworks. *Nat. Mater.* **21**, 924–931 (2022).
35. Mackrodt, W., Harrison, N., Saunders, V., Allan, N. & Towler, M. Direct evidence of O(p) holes in Li-doped NiO from Hartree–Fock calculations. *Chem. Phys. Lett.* **250**, 66 (1996).
36. Wolverton, C. & Zunger, A. First-principles prediction of vacancy order-disorder and intercalation battery voltages in Li_xCoO_2. *Phys. Rev. Lett.* **81**, 606 (1998).
37. Qiao, Z. et al. Informing geometric deep learning with electronic interactions to accelerate quantum chemistry. *Proc. Natl Acad. Sci.* **119**, e2205221119 (2022).
38. Barroso-Luque, L. et al. Cluster expansions of multicomponent ionic materials: formalism and methodology. *Phys. Rev. B* **106**, 144202 (2022).
39. Wang, Z. et al. Phase stability and sodium-vacancy orderings in a NaSICON electrode. *J. Mater. Chem. A* **10**, 209 (2022).
40. Reed, J., Ceder, G. & Ven, A. V. D. Layered-to-spinel phase transition in Li_xMnO_2. *Electrochem. Solid State Lett.* **4**, A78 (2001).
41. Kang, K. & Ceder, G. Factors that affect Li mobility in layered lithium transition metal oxides. *Phys. Rev. B* **74**, 094105 (2006).
42. Reimers, J. N., Fuller, E. W., Rossen, E. & Dahn, J. R. Synthesis and electrochemical studies of $LiMnO_2$ prepared at low temperatures. *J. Electrochem. Soc.* **140**, 3396–3401 (1993).

43. Koetschau, I., Richard, M. N., Dahn, J. R., Soupart, J. B. & Rousche, J. C. Orthorhombic LiMnO$_2$ as a high capacity cathode for Li-ion cells. *J. Electrochem. Soc.* **142**, 2906–2910 (1995).

44. Jang, Y.-I., Chou, F., Huang, B., Sadoway, D. R. & Chiang, Y.-M. Magnetic characterization of orthorhombic LiMnO$_2$ and electrochemically transformed spinel Li$_x$MnO$_2$(x<1). *J. Phys. Chem. Solids* **64**, 2525–2533 (2003).

45. Jo, M. R. et al. Triggered reversible phase transformation between layered and spinel structure in manganese-based layered compounds. *Nat. Commun.* **10**, 3385 (2019).

46. Radin, M. D., Vinckeviciute, J., Seshadri, R. & Van der Ven, A. Manganese oxidation as the origin of the anomalous capacity of Mn-containing Li-excess cathode materials. *Nat. Energy* **4**, 639–646 (2019).

47. Zhou, F., Maxisch, T. & Ceder, G. Configurational electronic entropy and the phase diagram of mixed-valence oxides: the case of Li$_x$FePO$_4$. *Phys. Rev. Lett.* **97**, 155704 (2006).

48. Walle, A. & Ceder, G. Automating first-principles phase diagram calculations. *J. Phase Equilibria* **23**, 348 (2002).

49. Delacourt, C., Poizot, P., Tarascon, J.-M. & Masquelier, C. The existence of a temperature-driven solid solution in Li$_x$FePO$_4$ for 0≤x≤1. *Nat. Mater.* **4**, 254–260 (2005).

50. Dodd, J. L., Yazami, R. & Fultz, B. Phase diagram of Li$_x$FePO$_4$. *Electrochem. Solid State Lett.* **9**, A151 (2006).

51. Xiao, Y. et al. Lithium oxide superionic conductors inspired by garnet and NASICON structures. *Adv. Energy Mater.* **11**, 2101437 (2021).

52. Huang, J. et al. Deep potential generation scheme and simulation protocol for the Li$_{10}$GeP$_2$S$_{12}$-type superionic conductors. *J. Chem. Phys.* **154**, 094703 (2021).

53. Lun, Z. et al. Cation-disordered rocksalt-type high-entropy cathodes for Li-ion batteries. *Nat. Mater.* **20**, 214–221 (2021).

54. Sun, Y. & Dai, S. High-entropy materials for catalysis: a new frontier. *Sci. Adv.* **7**, eabg1600 (2021).

55. Silvi, B. & Savin, A. Classification of chemical bonds based on topological analysis of electron localization functions. *Nature* **371**, 683–686 (1994).

56. King-Smith, R. & Vanderbilt, D. Theory of polarization of crystalline solids. *Phys. Rev. B* **47**, 1651 (1993).

57. Zhang, L. et al. A deep potential model with long-range electrostatic interactions. *J. Chem. Phys.* **156**, 124107 (2022).

58. Paszke, A. et al. in *Advances in Neural Information Processing Systems* (eds Wallach, H. et al.) 8026–8037 (Curran Associates, 2022).

59. Ong, S. P. et al. Python Materials Genomics (pymatgen): a robust, open-source python library for materials analysis. *Comput. Mater. Sci.* **68**, 314–319 (2013).

60. Larsen, A. H. et al. The atomic simulation environment—a Python library for working with atoms. *J. Phys. Condens. Matter* **29**, 273002 (2017).

61. Barroso-Luque, L. et al. smol: a Python package for cluster expansions and beyond. *J. Open Source Softw.* **7**, 4504 (2022).

62. Bitzek, E., Koskinen, P., Gähler, F., Moseler, M. & Gumbsch, P. Structural relaxation made simple. *Phys. Rev. Lett.* **97**, 170201 (2006).

63. He, X., Zhu, Y., Epstein, A. & Mo, Y. Statistical variances of diffusional properties from ab initio molecular dynamics simulations. *npj Comput. Mater.* **4**, 18 (2018).

64. Xie, F., Zhong, P., Barroso-Luque, L., Ouyang, B. & Ceder, G. Semigrand-canonical Monte-Carlo simulation methods for charge-decorated cluster expansions. *Comput. Mater. Sci.* **218**, 112000 (2023).

65. Deng, Z. et al. Phase behavior in rhombohedral NaSiCON electrolytes and electrodes. *Chem. Mater.* **32**, 7908 (2020).

66. Kresse, G. & Furthmüller, J. Efficiency of ab-initio total energy calculations for metals and semiconductors using a plane-wave basis set. *Computat. Mater. Sci.* **6**, 15–50 (1996).

67. Kresse, G. & Joubert, D. From ultrasoft pseudopotentials to the projector augmented-wave method. *Phys. Rev. B* **59**, 1758 (1999).

68. Perdew, J. P., Burke, K. & Ernzerhof, M. Generalized gradient approximation made simple. *Phys. Rev. Lett.* **77**, 3865–3868 (1996).

69. Wang, L., Maxisch, T. & Ceder, G. Oxidation energies of transition metal oxides within the GGA+U framework. *Phys. Rev. B* **73**, 195107 (2006).

70. Deng, B. Materials Project Trajectory (MPtrj) dataset. *figshare* https://doi.org/10.6084/m9.figshare.23713842 (2023).

71. Deng, B., Riebesell, J., Han, K., Barroso-Luque, L. & Zhong, P. Cedergroup hub/chgnet: v0.2.0. *Zenodo* https://doi.org/10.5281/zenodo.8173515 (2023).

Author contributions
B.D., P.Z. and G.C. conceived the initial idea. B.D. collected the datasets. B.D., J.R. and K.H. developed and formalized the code base. B.D., P.Z. and K.J. performed the simulations. P.Z., C.J.B. and G.C. offered insight and guidance throughout the project. B.D., P.Z. and G.C. prepared the paper. All authors contributed to discussions and approved the paper.

Competing interests
The authors declare no competing interests.

Additional information
Supplementary information The online version contains supplementary material available at https://doi.org/10.1038/s42256-023-00716-3.

Correspondence and requests for materials should be addressed to Peichen Zhong or Gerbrand Ceder.

Peer review information *Nature Machine Intelligence* thanks the anonymous reviewers for their contribution to the peer review of this work.

Reprints and permissions information is available at www.nature.com/reprints.

Publisher's note Springer Nature remains neutral with regard to jurisdictional claims in published maps and institutional affiliations.